The Astrophysical Journal, 976:131 (15pp), 2024 November 20 https://doi.org/10.3847/1538-4357/ad712f

Revealing the Elusive Companion of the Red Giant Binary 2MASS J05215658+4359220 from UV HST and Astrosat/UVIT Data

Luciana Bianchi[1,4], John Hutchings[2], Ralph Bohlin[3], David Thilker[1], and Emanuele Berti[1]
[1] Department of Physics & Astronomy, The Johns Hopkins University, 3400 N. Charles St., Baltimore, MD 21218, USA; bianchi@jhu.edu
[2] Herzberg Institute for Astrophysics, Victoria, Canada
[3] Space Telescope Science Institute, 3400 San Martin Dr., Baltimore, MD 21218, USA
Received 2024 June 5; revised 2024 August 15; accepted 2024 August 16; published 2024 November 22

Abstract

Black hole (BH) demographics in different environments is critical in view of recent results on massive star binarity, and of the multimessenger detectability of compact object mergers. But the identification and characterization of noninteracting BHs are elusive, especially in the sparse field stellar population. A candidate noninteractive BH + red giant (RG) binary system, 2MASS J05215658+4359220, was identified by T. A. Thompson et al. We obtained Astrosat/UVIT far-ultraviolet (FUV) imaging and Hubble Space Telescope (HST) UV−optical imaging and spectroscopy of the source to test possible scenarios for the optically elusive companion. HST/STIS spectra from ≈1600 to 10230 Å are best fit by the combination of two stellar sources, a RG with $T_{\rm eff} = 4250 \pm 150$ K, $\log g = 2.0$, $R_{\rm RG} \sim 27.8\,R_\odot$ (assuming a single-temperature atmosphere), and a subgiant companion with $T_{\rm eff} = 6000$ K, $R_{\rm comp} = 2.7\,R_\odot$, or $T_{\rm eff} = 5270$ K, $R_{\rm comp} = 4.2\,R_\odot$ using models with one-tenth or one-third solar metallicity, respectively, $\log g = 3.0$, extinction $E_{B-V} = 0.50 \pm 0.2$, adopting the Data Release 3 Gaia distance $D = 2463 \pm 120$ pc. No FUV data existed prior to our programs. STIS spectra give an upper limit of 10^{-17} erg cm^{-2} s^{-1} Å^{-1} shortwards of 2300 Å; an upper limit of $\gtrsim$25.7 ABmag was obtained in two UVIT FUV broad bands. The nondetection of FUV flux rules out a compact companion such as a hot white dwarf. The STIS spectrum shows strong Mg II λ2800 Å emission, typical of chromospherically active RGs. The masses inferred by comparison with evolutionary tracks, $\sim 1 M_\odot$ for the RG and between 1.1 and 1.6 $M_\odot$ for the subgiant companion, suggest past mass transfer, although the RG currently does not fill its Roche lobe. WFC3 imaging in F218W, F275W, F336W, F475W, and F606W shows an unresolved source in all filters.

Unified Astronomy Thesaurus concepts: Binary stars (154); Spectroscopic binary stars (1557); Companion stars (291); Stellar mass black holes (1611); Close binary stars (254); Red giant stars (1372); Subgiant stars (1646); Ultraviolet spectroscopy (2284); Ultraviolet photometry (1740)

1. Introduction: Noninteracting BHs Are Theoretically Predicted but Elusive

Finding and characterizing noninteracting stellar-mass black holes (BHs) is critical in view of the capability to detect multi-messenger signals from compact object mergers (e.g., K. A. Postnov & L. R. Yungelson 2006; B. P. Abbott et al. 2017a, 2017b, 2017c), and, on the other hand, of the growing evidence that the majority of massive stars are formed in binaries and that ∼70% of these binaries interact, with 20%–30% of them possibly merging (e.g., K. Abadie et al. 2010; H. Sana et al. 2014, 2017; M. Moe & R. di Stefano 2017; L. R. Patrick et al. 2019). These findings challenge our understanding of stellar evolution and stellar populations (e.g., B. P. Abbott et al. 2016). A missing critical ingredient in this scenario is an observational characterization of BH demographics: interacting and merging systems are a biased subset of the whole population, and mass measurements are currently obtained almost exclusively for pulsars and accreting binary systems selected from radio, X-ray, and gamma-ray surveys (e.g., F. Ozel et al. 2010, 2012; J. Antoniadis et al. 2016). Numerous studies focus on globular clusters (e.g., D. J. D'Orazio & J. Samsing 2018; S. Banerjee 2018), a special environment, where dynamical interactions can alter native statistics, resulting in an environment that is not representative of the stellar "field" and the young populations. For example, N. Langer et al. (2020) binary evolution models predict over 100 OB star−BH systems in the LMC, whereas only one (interacting, LMC X-1) is known.

2. A Wide Binary with an Optically Elusive Companion

A strong candidate binary comprised of a red giant (RG) and an unseen companion with inferred mass in the stellar BH regime was identified by T. A. Thompson et al. (2019, hereafter T2019) from a large (∼200) APOGEE stellar sample with high radial velocities. T2019 reported the RG to vary in radial velocity (RV; amplitude of 44.6 km s^{-1}) and optical brightness (V-mag amplitude of ∼0.2 mag) with a period of $P = 82.2 \pm 2.5$ days, and interpreted the synchronous light variation as due to spots in a locked rotation-orbital motion. From the optical-IR spectral energy distribution (SED), T2019 derived $T_{\rm eff} = 4530 \pm 89$ K, $E_{B-V} = 0.445 \pm 0.050$, $\log(L_{\rm bol}/L_\odot) = 2.52 \pm 0.03$, $\log g = 2.5$, $M \sim 3.2 \pm 1 M_\odot$ for the RG, using a distance of $D = 3106$ pc from Gaia Data Release 2 (DR2) corrected for binary motion. Gaia Data Release 3 (DR3) considerably revised this source's parallax, from $p = 0.322^{+0.075}_{-0.069}$ mas in DR2 to 0.399626 ± 0.015740 mas in DR3, bringing the distance to $D = 2.46 \pm 0.12$ kpc (as corrected by K. El-Badry et al. 2024, in preparation).

[4] http://dolomiti.pha.jhu.edu

In T2019's comprehensive SED analysis, which spans a wide wavelength range, one data point remained inconsistent: a detection of the source in near-UV (NUV), measured by both GALEX NUV and Swift UVOT.UVM2. T2019 showed that the archival NUV emission is incompatible with the RG SED, as expected, but also with an overall fit of the optical-IR SED if a main-sequence stellar companion were added to account for the NUV flux (see their Figure S8). Such conclusion, and the inferred companion mass, led T2019 to suggest a BH companion.

The source is included in two GALEX broadband NUV images, with $\mathrm{mag_{NUV}} = 21.49 \pm 0.36$ and $= 21.44 \pm 0.59$ in the AB system. We examined the GALEX data and confirmed the identification; we also dismiss a possible association of the GALEX NUV source with a very faint Gaia DR3 source at $\sim 3''$ away as unlikely. Five measurements with Swift UVOT.UVM2 (NUV range) were discussed by T2019. Archival NUV data are listed in Table 1. No far-ultraviolet (FUV) observations existed prior to our programs, presented in this work.

3. Unveiling the Elusive Companion and the Source of the NUV Flux

Given the relevance of a strong candidate for a binary system with a *noninteracting* BH companion, we felt it of great interest to test any possible alternative scenario that could explain the existing ample data; were alternatives ruled out, the BH hypothesis would gain strength. To this aim, we focused on the only unexplained measurements in the T2019 SED analysis: the NUV flux, detected consistently by two instruments. We considered the possible scenarios below, and obtained new data from FUV to optical wavelengths critical to conclusively test all of them.

3.1. Could a Hot White Dwarf or White Dwarf Pair Explain the NUV Excess?

3.1.1. Model Predictions

Among alternative explanations for the detected NUV flux, and possible scenarios for the optically elusive companion, we had estimated that both GALEX and Swift NUV fluxes could be compatible with a hot white dwarf (WD), or a WD close pair orbiting the RG at a larger separation (Figure 1). Their presence would not alter the RG optical-IR SED fit by T2019, but rule out the BH companion. To test such possibility we planned deep observations in FUV with Astrosat/UVIT (S. N. Tandon et al. 2020) and the Hubble Space Telescope (HST).

We used extensive model magnitude grids in UV and optical filters for hot WDs (Tlusty) and main-sequence and giant stars (Kurucz), sampling ranges of stellar parameters and reddening (L. Bianchi 2024, in preparation). Owing to the broadness of the filters' passband in the NUV archival data, which include the 2175 Å absorption, model atmosphere spectra were reddened progressively, with different types of extinction curves, and then synthetic model magnitudes were computed in GALEX, Swift, UVIT, HST, and other optical filters. Figure 1 shows sequences of WD model magnitudes ($T_{\rm eff} = 15$ k to 200 kK, $\log g = 7$) scaled to the target distance of 2463 pc, for two plausible WD radii, 0.02 and $0.03 R_\odot$, and reddened with a few illustrative values of E_{B-V}: 0.45 mag using reddening curves with $R_V = 3.1$ (Milky Way type) or $R_V = 2.0$, to show the effect of the adopted reddening curve on UV fluxes, and $E_{B-V} = 0.55$ mag ($R_V = 3.1$) and 0.50 mag ($R_V = 2.0$) to show two examples compatible with the observed GALEX-Swift NUV color (vertical line). A different adopted distance would translate into a corresponding change in radius, for the same magnitude, given that flux scales as R^2/D^2, and a pair of identical WDs of course would be 0.75 mag brighter (twice the flux) than a single WD. Figure 1 shows that the measured GALEX and Swift NUV fluxes, unexplained by T2019's scenario and by subsequent works, *could be compatible* with a hot WD, or a WD pair, with reddening as derived by T2019 or higher. However, the NUV data alone are not sufficient to confirm a possible WD, nor to derive its $T_{\rm eff}$, $\log g$, radius (hence $L_{\rm bol}$), as the solution strongly depends on E_{B-V}. Additional FUV colors would be needed to constrain the solution, but no FUV data existed for this source (the GALEX FUV detector was off during the exposures, and only NUV images were acquired).

3.1.2. Astrosat/UVIT FUV Observations and Measurements, and Results

Therefore, we obtained Astrosat/UVIT imaging in two FUV filters, the very broad FUV.CaF2 (F148W; $\lambda_{\rm eff} = 1481$ Å, $\Delta\lambda = 500$ Å) and the medium-width FUV.Sapphire (F169M; $\lambda_{\rm eff} = 1608$ Å, $\Delta\lambda = 290$ Å). Two UVIT proposals were approved (A09_058 and A10_093; PI: Bianchi). An exceptionally large allocation of observing time was granted to repeat deep exposures sampling orbital phases, but only part of the approved observations were eventually executed, due to a number of scheduling issues and delays. The observations are listed in Table 2. The UVIT data were reduced with the s/w package of J. E. Postma & D. Leahy (2021), which reconstructs the images from the photon-counting data and precisely estimates the effective exposure time accounting for dead-time corrections during the exposures. The source is not detectable in any of the images. Based on sky counts at the location of the source (using a 4 pixel radius aperture, sky radii 8–10 pixels and 100 randomly placed apertures in the vicinity of the source), we obtained 2σ upper limits of >25.8 ABmag for FUV.CaF2 ($\sim 2.3 \times 10^{-18}$ erg cm^{-2} s^{-1} Å^{-1} at $\lambda_{\rm eff}$) and >25.7 ABmag ($\sim 2.2 \times 10^{-18}$ erg cm^{-2} s^{-1} Å^{-1} at $\lambda_{\rm eff}$) for FUV.Sapphire. These limits are ≈ 4 mag fainter than the GALEX NUV measurements, and of the NUV fluxes in our HST data (Section 3.2.1).

The FUV upper limits rule out the presence of a hot stellar source (see, e.g., FUV–NUV model colors in L. Bianchi & B. Shiao 2020 and L. Bianchi 2024). Although a hot WD is not present in this case, we show the model predictions (Figure 1) as they may be useful for planning observations in other similar cases. The UVIT images, reconstructed from the photon-counting data, are made publicly available online (Section 5).

3.2. Can a Nondegenerate Stellar Companion Account for the NUV Flux?

A main-sequence stellar companion was ruled out by T2019's SED analysis of the then-available data (albeit with the unaccounted discrepancy in the archival GALEX and Swift NUV broadband fluxes, as we noted), based on the argument that if a companion of mass $\sim 3.3 M_\odot$ were a nondegenerate star, its luminosity would be detectable in the SED. An alternative scenario was proposed by E. P. van den Heuvel & T. M. Tauris (2020, hereafter VdHT20), who suggested that a close pair of K0-4V stars ($2 \times 0.9 M_\odot$) could

Table 1
Archival NUV Measurements for 2MASS J05215658+4359220[a]

Instrument and Filter	Observation ID	R.A., Decl. Center	Start Date	End Date	Exp. Time (s)	Mag
GALEX NUV	AIS_57_1_69[b]	05:21:56.760 +43:59:22.03	2012-01-5	2012-01-5	96.00 (65.89)	21.44 ± 0.59 ABmag
GALEX NUV	AIS_57_1_75[b]	05:21:56.610 +43:59:22.01	2012-01-5	2012-01-5	103.05 (70.67)	21.49 ± 0.36 ABmag
UVOT UVM2[c]	00010442002	05 22 05.240 +43 59 44.54	2018-08-09 08:23:52	2018-08-09 10:14:56	1435.612 (2)	>20.27 Vegamag
UVOT UVM2[c]	00010442003	05 22 01.996 +43 59 19.90	2018-08-10 19:30:19	2018-08-11 10:10:55	2791.814 (4)	19.75 ± 0.21 Vegamag
UVOT UVM2[c]	00010442004	05 21 59.182 +43 59 02.73	2018-08-12 23:59:49	2018-08-13 01:47:55	2101.318 (2)	20.22 ± 0.21 Vegamag
UVOT UVM2[c]	00010442005	05 22 01.732 +43 57 24.03	2018-08-15 01:35:49	2018-08-15 06:36:55	2068.513 (3)	19.90 ± 0.19 Vegamag
UVOT UVM2[c]	00010442006	05 21 58.697 +43 58 23.97	2018-09-08 00:51:26	2018-09-08 10:20:52	1999.570 (6)	20.06 ± 0.22 Vegamag
UVOT U[c]	00010442006	05 21 58.697 +43 58 23.97	2018-09-08 00:58:05	2018-09-08 10:22:56	1920.615 (6)	19.77 ± 0.18 Vegamag

Notes.
[a] For a compilation of other data at longer wavelengths, see K. El-Badry et al. (2024, in preparation).
[b] In the first and second rows, respectively: IAU name: GALEX J052156.7+435922 and GALEX J052156.6+435922, GALEX objid = 6372921338785432248 and 6372921345227885710, GALEX photoetxractid = 6372921338784382976 and 6372921345226833920 in the GALEX database.
[c] From T2019; Target name: BR0521_4359.

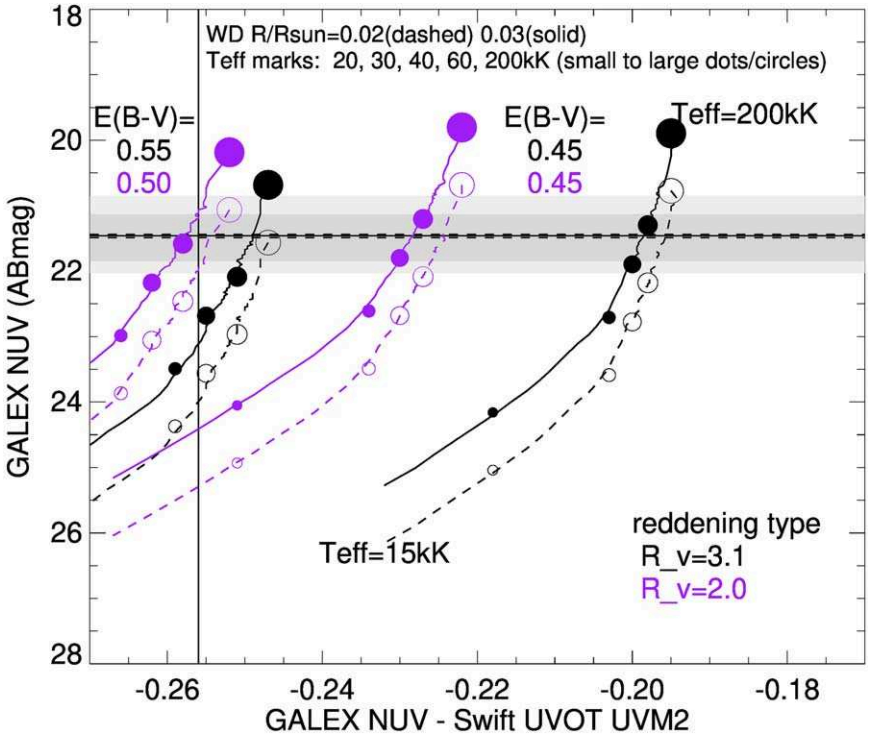

Figure 1. Model magnitude–color sequences for a WD of $T_{\rm eff}$ = 15 kK to 200 kK with radii of R = 0.03 and 0.02 $R_{\odot}$ at the distance of the target. A pair of identical WDs would be shifted upward correspondingly to twice the flux, i.e., by 0.75 mag. The target's measured GALEX NUV magnitudes are shown with horizontal dashed lines (gray shadowed areas show the uncertainties), and the NUV − UVM2 color with a vertical line. Model magnitudes are reddened with two different extinction types (R_V = 3.1, black; R_V = 2, purple sequences) and different amounts of extinction, for illustration purposes. The plot shows that (i) a WD or WD pair (or a cooler main-sequence star, not shown) could account for the GALEX and Swift NUV measurements, unexplained by a red giant SED (ii) from NUV-only data, $T_{\rm eff}$ is degenerate with radius and E_{B-V}; therefore, FUV imaging and a UV−optical spectrum were obtained to test the presence of a hot companion and to constrain its parameters if present.

account for the inferred companion mass and have a combined luminosity compatible with the overall SED presented by T2019. Such a scenario would account for the companion's presumed mass, but not for the NUV flux, while our proposed alternatives would (Section 3.1 and here below). VdHT20 also suggested a $1M_{\odot}$ RG primary to be more plausible, given the lack of X-ray emission and the surface chemistry of the RG. T. Thompson et al. (2020, hereafter T2020) responded with arguments favoring a $3.2^{+1}_{-1}M_{\odot}$ RG primary, considering the luminosity. The new parallax from Gaia DR3 places the object significantly closer than Gaia DR2, at about 80% of the distance used by T2019, implying a downward revision of the RG's luminosity and radius.

The presence and the nature of a stellar companion that could account for both the inferred mass ratio in the system and the archival NUV fluxes were successfully tested, and we believe conclusively proven, by HST UV−optical STIS spectroscopy described below.

3.2.1. HST STIS Spectroscopy

We obtained HST/STIS spectra covering a very wide range from ∼1600 to 10230 Å, by using three STIS gratings: G230L, G430L, and G750L (dispersion = 1.58, 2.73, and 4.92 Å pixel^{-1}, respectively). Details of the observations are given in Table 3. The main objective was to obtain a UV spectrum, given that information in this wavelength range was critically missing from all previous studies. The addition of the optical spectrum with the G430L and G750L gratings provided simultaneous coverage at longer wavelengths, enabling robust and consistent modeling of the entire binary system. Combining UV and optical spectra taken at different times would make the results inconclusive, given the known flux variability of the RG in the V band, both with orbital period and long-term variations. In the original proposal, we had envisaged using the STIS grism to cover at once also the FUV range; however, after the HST proposal was approved and before Phase 2 was finalized, our UVIT observations had already started (Section 3.1.2), showing no FUV fluxes at the expected level in the hot-WD companion hypothesis (Section 3.1). Therefore, we switched the configuration to the G230L grating, which yields a much better signal-to-noise ratio (S/N) in the range where flux from the source was expected, and was indeed detected (Figures 2–5). The STIS data reduction followed the procedure used for the CALSPEC database.[5] The extracted combined STIS spectrum is also made available in electronic form (Section 5).

3.2.2. Modeling the STIS Spectra: Parameters of the Stellar Pair

The STIS spectrum, shown in Figures 2–4, was analyzed with Kurucz models.[6] To fit the whole spectrum, which is the sum of two components, each one depending on several parameters, and both affected by reddening, whose effect is significantly wavelength dependent because the spectral range spans from UV to IR, we anchored the model fluxes to average continuum flux values computed in small regions of the

[5] http://www.stsci.edu/hst/instrumentation/reference-data-for-calibration-and-tools/astronomical-catalogs/calspec

[6] We used the grid of Kurucz models by F. Castelli & R. L. Kurucz (2003).

Table 2
Astrosat/UVIT Observations and Resulting Measurements for 2MASS J05215658+4359220

Instrument and Filter	Observation ID[a]	Data Set	Date (Mean HJD)	Exp. Time[b] (s)	Mag (ABmag)
UVIT FUV.F1 (CaF2)	A10_093T01_9000004	A10_093T01_9000004128	2459236.3073659	4133.383	>25.0[c] (2σ)
UVIT FUV.F1 (CaF2)	A10_093T01_9000004	A10_093T01_9000004266	2459291.7881458	4251.031	…
UVIT FUV.F1 (CaF2)	A10_093T01_9000004	Merged	…	8384.415	>25.8[d] (2σ)
UVIT FUV.F3 (Sapphire)	A10_093T01_9000004	A10_093T01_9000004128	2459236.3219791	6561.54	>24.5[c] (2σ)
UVIT FUV.F3 (Sapphire)	A10_093T01_9000004	A10_093T01_9000004266	2459291.85908	6865.869	…
UVIT FUV.F3 (Sapphire)	A10_093T01_9000004	Merged	…	13427.442	>25.7[d] (2σ)

Notes.
[a] Bianchi's program A10_093.
[b] RDCDTIME (physical integration times for images, reduced for parity errors, cosmic rays, and missing frames).
[c] 2σ upper limit, obtained by measuring countrates of 100 random apertures in the target position and nearby, for aperture size = 3 pixels (approximately 3″). For an aperture size of 5 pixels we obtain upper limits about half-magnitude brighter. Correction for the fraction of flux in the aperture is applied following S. N. Tandon et al. (2020); no extinction correction is applied.
[d] A 4 pixel radius was used for measurements on merged images.

spectrum rather free of lines. We started with regions in the longest wavelength part of the spectrum where the companion flux is negligible (about 0.6% or 6% of the RG flux, according to our decomposition in Figures 2 and 3, metallicity $Z = 0.002$ and $Z = 0.006$, respectively); the flux of each model with a given $T_{\rm eff}$ (and $\log g$, metallicity) was anchored to the RG observed flux in a long-wavelength continuum region, and E_{B-V} was varied—for each model—in an ample range with small steps; a value was constrained from the slope that best matches the overall shape of the spectrum at long wavelengths and does not exceed the observed fluxes where the companion's flux becomes relevant. A companion's contribution to the total flux was eventually estimated to be $\lesssim$18% or 32% (for the two metallicity values shown) shortwards of ~4000 Å, and overwhelming the RG flux shortwards of ~3000 Å, as can be seen in Figures 2–4. The relative contributions in these regions depend on the model parameters of both stars, and the best match across the whole wavelength range is achieved with iterations. The comparison of broad absorption bands in the respective models gives a qualitative indication of metallicity and gravity, as shown by the differences between Figures 2 versus 3, and in Figure 4, top versus bottom panel. The solution could be further constrained if metallicity and gravity were precisely derived from high-resolution, high-S/N line analysis spectra, which should be possible at least for the RG (K. El-Badry et al. 2024, in preparation).

Adopting the Gaia DR3 distance of $D = 2463$ pc, the best overall fit of both continuum and main absorption bands across the entire range of the combined STIS spectra (1600−10230 Å) is obtained by the sum of two stars: a red giant with $T_{\rm eff} = 4250$ K, $\log g = 2.0$, $R_{\rm RG} = 27.9 R_{\odot}$, and a companion with $T_{\rm eff} = 6000$ K, $\log g = 3.0$, $R_{\rm comp} = 2.7\,R_{\odot}$, using models with metallicity of one-tenth the solar value, that better match the main absorption features in the UV and blue range (see bottom panels in Figures 2 and 3, and Figure 4). Using models with metallicity $Z = 0.006$, the closest value in the model grid to the metallicity inferred by T2019 and by others from line analysis in ground-based spectra, the RG parameters hardly change ($R_{\rm RG} = 27.78 R_{\odot}$), but parameters of the companion require $T_{\rm eff} = 5750$ K and $R_{\rm comp} = 4.2 R_{\odot}$ to match the UV region, where the RG flux varies the most with metallicity (Figure 4). The values of $\log g$ were initially fixed from the preliminary line analysis by K. El-Badry (2024, private communication) of high-resolution, high-S/N Keck spectra since those data are more sensitive to this parameter; however, we then varied also $\log g$ values and could not obtain an equally good SED fit across the whole spectral range by adjusting other parameters. Extinction was constrained at $E_{B-V} = 0.50 \pm 0.02$ mag; small changes would cause large discrepancies in the shortest wavelength part of the spectrum, or inconsistencies across the entire available range, which could not be compensated by variations of $T_{\rm eff}$ or other parameters.

The STIS spectral coverage extending to UV wavelengths allowed us to refine the stellar parameters of the hotter companion better than is possible from other studies, while the RG parameters obtained from the Keck spectra line analysis (K. El-Badry 2024, private communication) were essentially confirmed. The comparison of two different solutions in Figure 4 illustrates the unique leverage of the UV spectral portion for achieving a consistent solution of all parameters, including stellar radii, as well as the need to constrain metallicity and gravity from high-resolution line analysis, in order to further restrict the acceptable combinations of parameters.

The extracted STIS spectrum, convolved with the GALEX NUV transmission curve, yields a synthetic GALEX NUV magnitude of 21.45 ABmag (19.77 in the Vegamag system). The value is in perfect agreement with the GALEX archival measurements, in spite of the latter having large uncertainties because the source is included only in GALEX images with very short exposures (Table 1).

3.3. Chromospheric Line Emission from the Red Giant

When planning the HST spectroscopy, we had also estimated whether chromospheric and transition zone line emission from an active RG could possibly be sufficient to account for the GALEX and Swift NUV broadband flux. A nondetection of UV continuum flux, ruling out a stellar companion(s) or an accretion disk, would have favored the most exciting among the possible scenarios: it would have confirmed a noninteracting BH as the companion to the RG. We had gauged the likelihood of this scenario by scaling nearby "analogs" of the RG primary with existing archival spectra, and found it unlikely to account for the measured NUV fluxes. The STIS spectral exposure proved to be adequate to test our different postulated scenarios; the spectra, analyzed in the previous section, show with good S/N both the continuum flux and

Table 3
HST Observations (Bianchi's Program HST-GO-16654)

Data Set	Target ID	R.A.	Decl.	Start Time	End Time	Exp. Time (s)	Instr.	Aperture	Filter/ Grating	Central λ
				HST Imaging						
IEMQA1010	2MASS J05215658 +4359220	80.48579541667	43.98943333333	2022-04-17T07:33:34.060	2022-04-17T07:58:10.583	0.96	WFC3	UVIS2-C1K1C-SUB	F606W	5887.7124
IEMQA1020	2MASS J05215658 +4359220	80.48579541667	43.98943333333	2022-04-17T07:35:20.073	2022-04-17T07:59:56.760	1.39	WFC3	UVIS2-C1K1C-SUB	F475W	4772.1709
IEMQA1030	2MASS J05215658 +4359220	80.48579541667	43.98943333333	2022-04-17T07:37:21.067	2022-04-17T08:03:44.057	20.0	WFC3	UVIS2-C1K1C-SUB	F336W	3354.6558
IEMQA1031	2MASS J05215658 +4359220	80.48579541667	43.98943333333	–2022-04-17T07:37:21.067	2022-04-17T07:39:08.057	10.0	WFC3	UVIS2-C1K1C-SUB	F336W	3354.6558
IEMQA1032	2MASS J05215658 +4359220	80.48584915326	43.98944463119	2022-04-17T08:01:57.067	2022-04-17T08:03:44.057	10.0	WFC3	UVIS2-C1K1C-SUB	F336W	3354.6558
IEMQA1040	2MASS J05215658 +4359220	80.48579541667	43.98943333333	2022-04-17T07:41:08.073	2022-04-17T08:13:22.073	528.0	WFC3	UVIS2-C1K1C-SUB	F218W	2223.7244
IEMQA1041	2MASS J05215658 +4359220	80.48579541667	43.98943333333	2022-04-17T07:41:08.073	2022-04-17T07:48:46.073	264.0	WFC3	UVIS2-C1K1C-SUB	F218W	2223.7244
IEMQA1042	2MASS J05215658 +4359220	80.48584915326	43.98944463119	2022-04-17T08:05:44.073	2022-04-17T08:13:22.073	264.0	WFC3	UVIS2-C1K1C-SUB	F218W	2223.7244
IEMQA1050	2MASS J05215658 +4359220	80.48579541667	43.98943333333	2022-04-17T07:50:46.090	2022-04-17T08:20:49.080	460.0	WFC3	UVIS2-C1K1C-SUB	F275W	2703.2976
IEMQA1051	2MASS J05215658 +4359220	80.48579541667	43.98943333333	2022-04-17T07:50:46.090	2022-04-17T07:56:13.080	230.0	WFC3	UVIS2-C1K1C-SUB	F275W	2703.2976
IEMQA1052	2MASS J05215658 +4359220	80.48584915326	43.98944463119	2022-04-17T08:15:22.057	2022-04-17T08:20:49.080	230.0	WFC3	UVIS2-C1K1C-SUB	F275W	2703.2976
OEMQ01MIQ[a]	2MASS J05215658 +4359220	80.48579541667	43.98943333333	2022-04-17T04:23:12.010	2022-04-17T04:26:13.167	3.1	STIS	F28X50LP	MIRVIS	0.0
				HST Spectroscopy						
OEMQ01010	2MASS J05215658 +4359220	80.48579541667	43.98943333333	2022-04-17T04:31:38.987	2022-04-17T04:43:45.987	727.0	STIS	52 × 0.5	G230L	2376.0
OEMQ01020	2MASS J05215658 +4359220	80.48579541667	43.98943333333	2022-04-17T04:46:03.977	2022-04-17T04:57:31.977	600.0	STIS	52 × 0.5	G430L	4300.0
OEMQ01030	2MASS J05215658 +4359220	80.48579541667	43.98943333333	2022-04-17T05:03:12.970	2022-04-17T05:09:40.970	300.0	STIS	52 × 0.5	G750L	7751.0
OEMQ01050	2MASS J05215658 +4359220	80.48579541667	43.98943333333	2022-04-17T05:57:59.977	2022-04-17T06:44:29.977	2790.2	STIS	52 × 0.5	G230L	2376.0
OEMQ01040[b]	None	80.3780550487	44.02705481179	2022-04-17T05:13:16.970	2022-04-17T05:18:38.953	240.0	STIS	0.3 × 0.09	G750L	7751.0

Notes.
[a] Acquisition Image for STIS spectroscopy.
[b] Fringe flat for the G750L. "None" indicates that there was no external target, just the internal tungsten lamp.

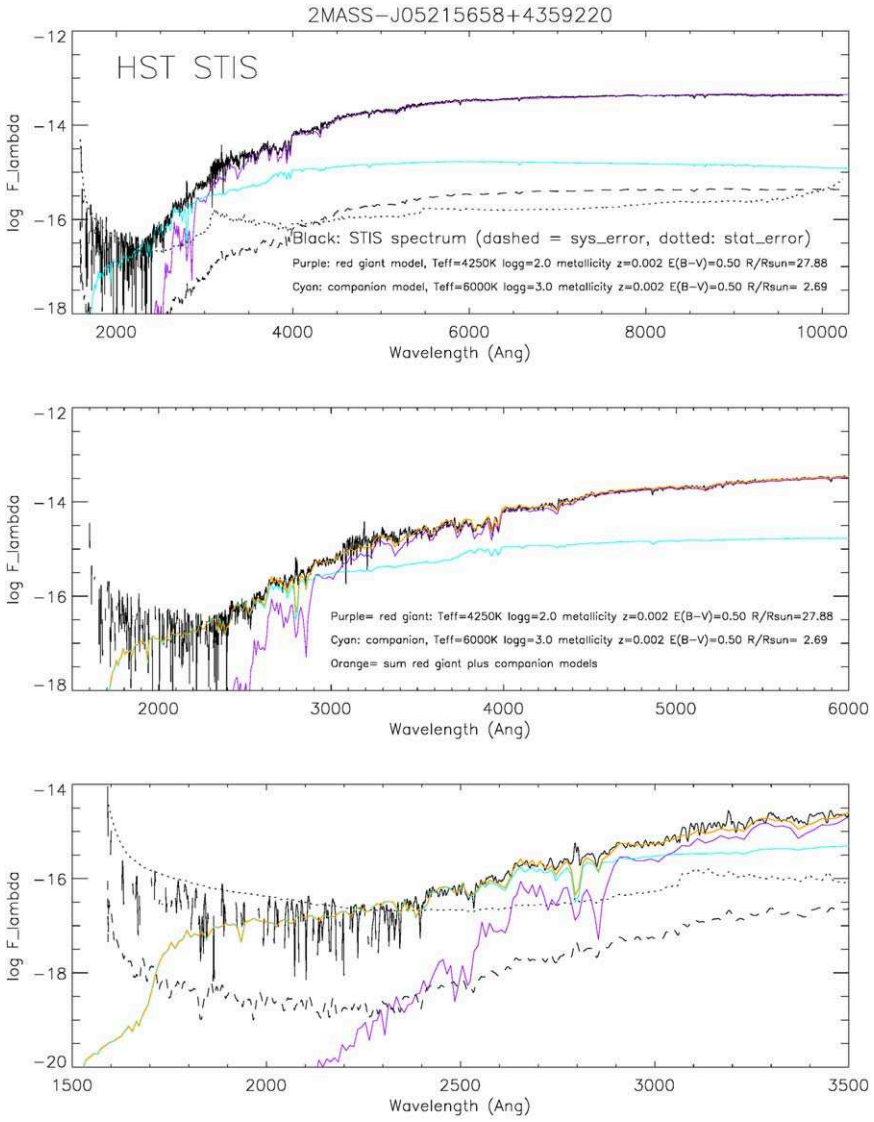

Figure 2. STIS UV+optical spectra (G230L+G430L+G750L combined, flux in erg cm^{-2} s^{-1} Å^{-1}) plotted in black, with the best-fit two-component stellar models: $T_{\rm eff} = 4250$ K, log $g = 2.0$ for the RG (purple), and $T_{\rm eff} = 6000$ K, log $g = 3.0$ for the companion (cyan). A metallicity of 10 times less than solar provides the best match to all major spectral features for the derived log g, and an extinction of $E_{B-V} = 0.5$ (assuming a Milky Way–type extinction, with $R_V = 3.1$) yields the overall best match to the SED across the whole range. The summed flux of the two models is shown in orange (middle and bottom panels). With the Gaia DR3 distance, scaling the best-fit-model fluxes to the STIS fluxes accounting for the derived extinction, yields radii of $R_{\rm RG} = 27.8$ and $R_{\rm comp} = 2.7\ R_{\odot}$. In the top and bottom panels the systematic error (dashed line) and statistical error (dotted lines) of the STIS spectra are also shown. Shortwards of ∼2400 Å the data yield only an upper limit to the flux (see Figure 5).

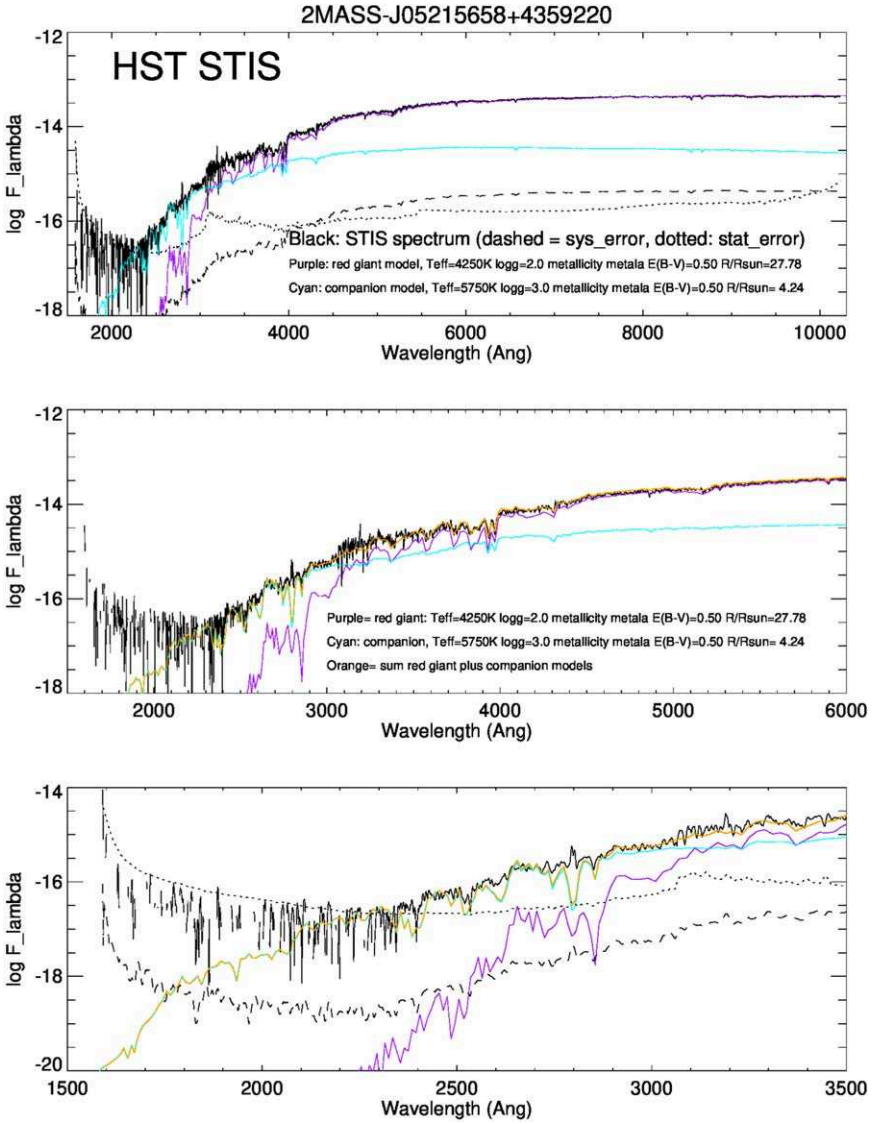

Figure 3. As in the previous figure: STIS UV+optical spectra (G230L+G430L+G750L combined, flux in erg cm^{-2} s^{-1} Å^{-1}) plotted in black, with the best-fit two-component stellar models, using models with metallicity $Z = 0.006$: The RG results do not differ from the previous case except for a slightly lower radius: $T_{\rm eff} = 4250$ K, log $g = 2.0$, and $R_{\rm RG} = 27.7 R_{\odot}$ (purple model), but a worse fit of broad line features is seen between 3000 and 4000 Å, largely compensated by adjusting the companion's parameters: $T_{\rm eff} = 5750$ K, log $g = 3.0$, and $R_{\rm comp} = 4.2 R_{\odot}$ (cyan model). Extinction of $E_{B-V} = 0.5$ still yields the best solution. The summed flux of the two models is shown in orange (middle and bottom panels). In the top and bottom panels the systematic error (dashed line) and statistical error (dotted lines) of the STIS spectra are also shown.

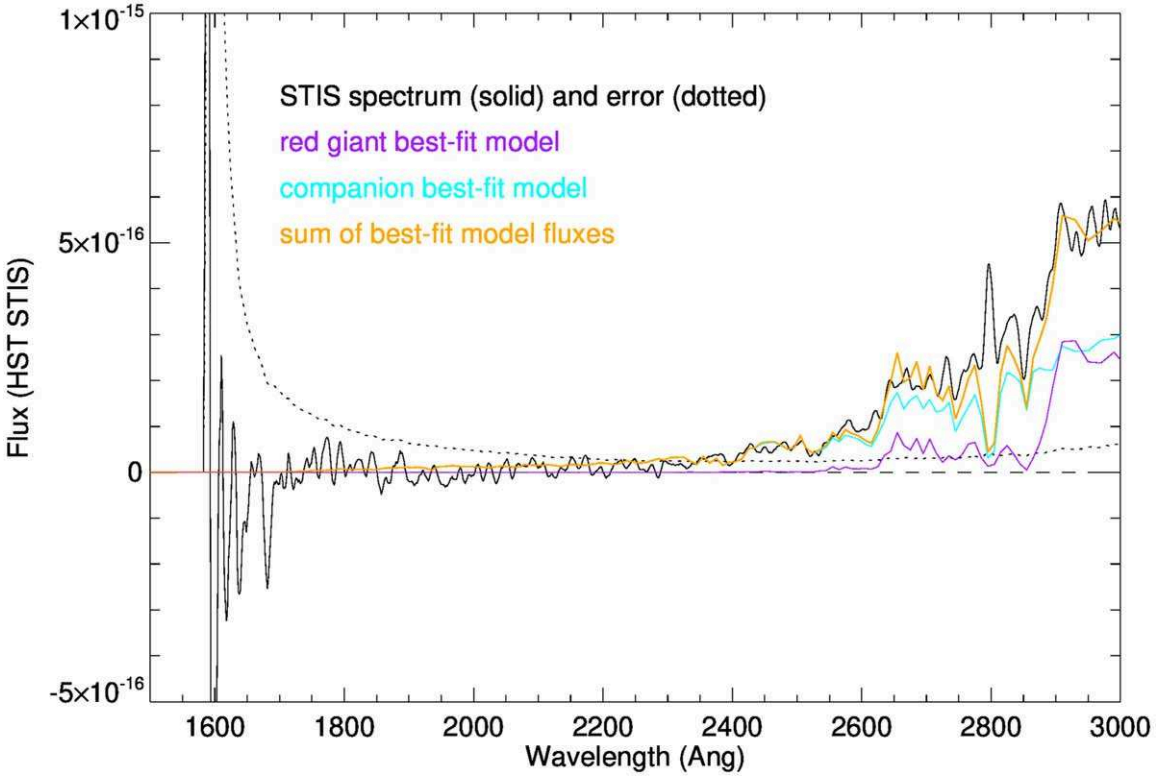

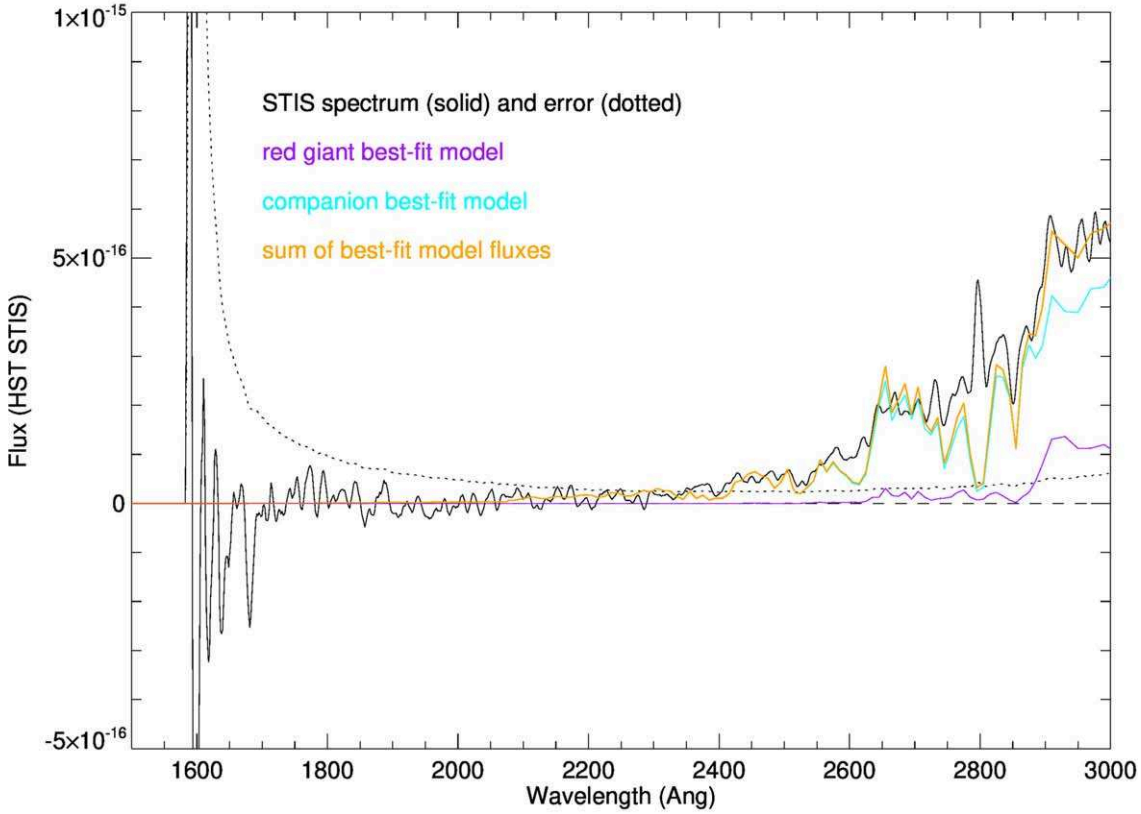

Figure 4. The shortest wavelength portion of the STIS spectrum, here with flux (erg cm^{-2} s^{-1} Å^{-1}) plotted in linear scale to better distinguish significant flux from noise level, and to illustrate the sensitivity of this range to the companion, whose flux becomes stronger than the RG's flux. Without this spectral region, the rest of the spectrum could be fit by a wider combination of $T_{\rm eff}$ and E_{B-V} values for the stellar pair. Models with metallicity $Z = 0.002$ are used in the top panel, and $Z = 0.006$ in the bottom panel, as in Figures 2 and 3, respectively. The different metallicity hardly affects the RG continuum flux over a wide optical-IR range, as shown in the two previous figures, but the difference becomes significant in this range, where the fit to the composite spectrum is compensated by the companion's solution, requiring a radius of 4.2 $R_\odot$ in the lower plot vs. 2.7 $R_\odot$ in the upper plot, and a slightly cooler $T_{\rm eff}$.

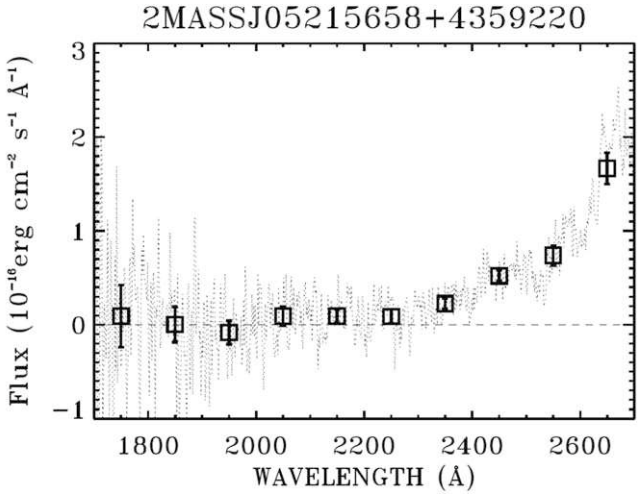

Figure 5. The STIS G230L combined data sets oemq01010+oemq01050 (dotted line) are consistent with an upper limit of 10^{-17} erg cm^{-2} s^{-1} Å^{-1} shortwards of ∼2300 Å. The squares are averages in 100 Å bins.

absorption lines of a stellar companion hotter than the RG, as well as chromospheric emission from the RG. The Mg II doublet at $\lambda \sim 2800$ Å, seen in emission in the STIS spectra, is shown in Figures 4 and 6. Measuring the emission flux above the local continuum would be misleading, given the presence of the same transitions in absorption in both the RG and the companion spectrum (see Figures 2 and 4, purple and cyan models), and the current uncertainty of the model fits in metallicity and gravity would propagate on the flux measurement. Instead, we compared the Mg II emission seen in the STIS spectrum with that of a possible analog, sufficiently near that UV archival spectra are available. UZ Lib (K0III) is an active RS CVn variable, possibly of the FK Comae class (e.g., K. G. Strassmeier 2009), with some stellar parameters similar to 2MASS J05215658+4359220; it also displays photometric variations of similar amplitude, although it has a shorter orbital period. For UZ Lib two archival International Ultraviolet Explorer (IUE) spectra in the NUV range exist; they show strong Mg IIλ2800 emission. Some apparent continuum flux at the long-wavelength end of the IUE spectral range is likely a red leak. Given the difference in reddening and distance between the two systems, in resolution between IUE low-resolution (∼6 Å) and STIS G230L, and the additional caveat that the NUV flux of 2MASS J05215658+4359220 has a major contribution by the hotter companion, overwhelming the RG continuum in this range (Figure 4), we scaled the UZ Lib IUE spectra such that the local continuum surrounding the Mg II emission matches the STIS flux level of 2MASS J05215658+4359220. The Mg II emission is apparently stronger in UZ Lib, by a factor of about 2 (Figure 6). But if the companion's contribution to the flux (cyan models in Figure 4) were subtracted from the STIS spectrum of 2MASS J05215658+4359220, the RG's Mg II emission would appear stronger than in UZ Lib.

Assessing whether the analogy of the RG chromospheric activity extends to the variability characteristics of UZ Lib type variables or the FK Comae class, where spot activity is enhanced in one hemisphere, related to binary interaction of a close or coalescing pair, would require UV observations at different orbital phases to monitor possible variability. We have limited our HST proposal to a one-time observation, given that the exposure times across the entire spectral range, but especially the UV, were estimated based on various scenarios that we had postulated, and calculated hypothetically, and it would not have been worth risking more observing time until the exposure times were proven appropriate by the first observations presented here.

3.4. Morphology: HST WFC3 Imaging Data

HST/WFC3 imaging was acquired in filters F218W, F275W, F336W, F475W, and F606W. The filter choice and exposures were tuned to optimize the derivation of physical parameters and extinction for a range of possible stellar companions based on simulations with our model grids. In particular, two UV filters are indispensable to disentangle E_{B-V} and $T_{\rm eff}$ if the companion were a hot stellar source (e.g., L. Bianchi et al. 2014). WFC3 does not have FUV filters, thus F218W and F275W were included. The WFC3 imaging was obtained to measure broad-band fluxes at wavelengths extending to NUV down to the faintest limits we could predict, given that the STIS spectroscopic exposures were estimated based on postulated scenarios yet to be tested, including the presence of a stellar companion hotter than the RG, but whose $T_{\rm eff}$ (or even presence) was in fact not predictable with previous data. We only imaged a small area around the target, using the UVIS2-M1K1C subarray option, which significantly reduces buffer dumps, and allowed us to accommodate all exposures in one orbit, at the expense of complicating the photometric measurements due to the lack of field stars to individually determine the point-spread function (PSF) in each image. Exposures were dithered, for mitigation of hot pixels and cosmetic defects in the array. Exposures in the red filters were split in very short exposures (using the charge transfer efficiency mitigation strategy) so as not to saturate the RG primary. Details of all HST data are compiled in Table 3. Given the good quality of the STIS spectra across the entire range, and the difficulty in obtaining precise photometry from the subarray images, the analysis to derive stellar parameters was performed only on the STIS spectra, which contain information on both continuum fluxes and line features. A portion of the WFC3 images around the target is shown in Figure 7; they are the highest-resolution imaging available of the source and its surroundings from 218 to 606 nm, providing information on the morphology, and they further confirm that the source of the UV flux is not an unrelated neighbor.

The WFC3 images in Figure 7 are arranged from the shortest to the longest effective wavelength of the filters (left to right panels). The images are repeated in subsequent rows, with different contrasts, to make more details appreciable; in each row we keep the same contrast relative to the background in all filters, to visualize the large dynamic range in flux across the sampled wavelength spectrum. Again the lack of other field sources in the images, preventing derivation of image-specific PSF, makes it difficult to examine whether the source is slightly resolved, or not pointlike, in F275W or F366W, where its flux is expected not to be completely overwhelmed by the RG, according to the STIS spectra. For a quantitative analysis of the source morphology, custom 4×-oversampled PSFs from the WFC3 PSFSTD libraries for each filter (or the closest filter in effective wavelength to the observed one) were created, as appropriate for the true detector position taking into consideration the placement of the subarray and source. Then *photutils* (Python) was used to do PSF-fitting photometry, a single pass of detection was run to measure objectively whether there was

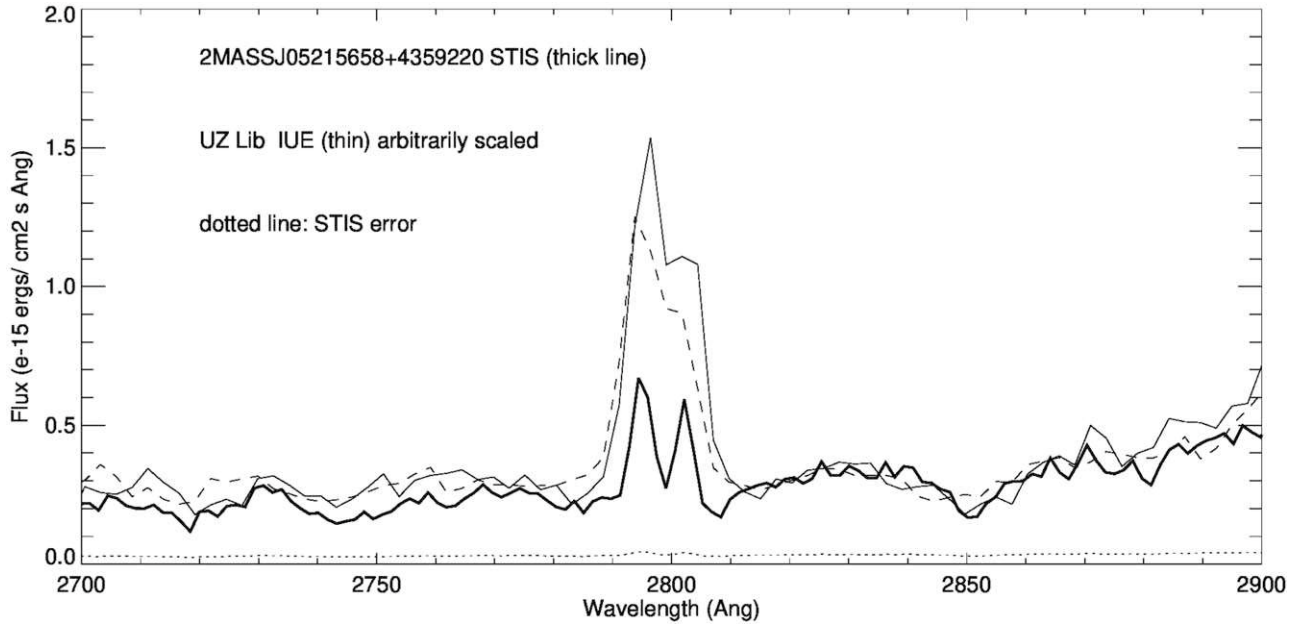

Figure 6. Mg II doublet emission in the STIS G230L spectrum of 2MASS J05215658+4359220 (thick line) compared with two IUE spectra of UZ Lib, a chromospherically active RG (thin solid and dashed lines). The fluxes of each IUE spectrum (LWP5711 and LWP5764) have been scaled to match the local continuum level of our target around the Mg II line. A caveat must be considered in the comparison: in 2MASS J05215658+4359220 the companion significantly contributes to the flux at these wavelengths (Figures 2 and 3 bottom panel, and Figure 4); subtracting its contribution (cyan models in Figure 4) would make the Mg II emission much stronger. A simple scaling by radius and distance is not possible because differential reddening should also be accounted for, which is uncertain for UZ Lib. Although sampled with a ∼2.66 Å step, the IUE spectra have an actual resolution of ∼6 Å, lower than the STIS G230L spectra. The STIS resolution has not been degraded in the plot.

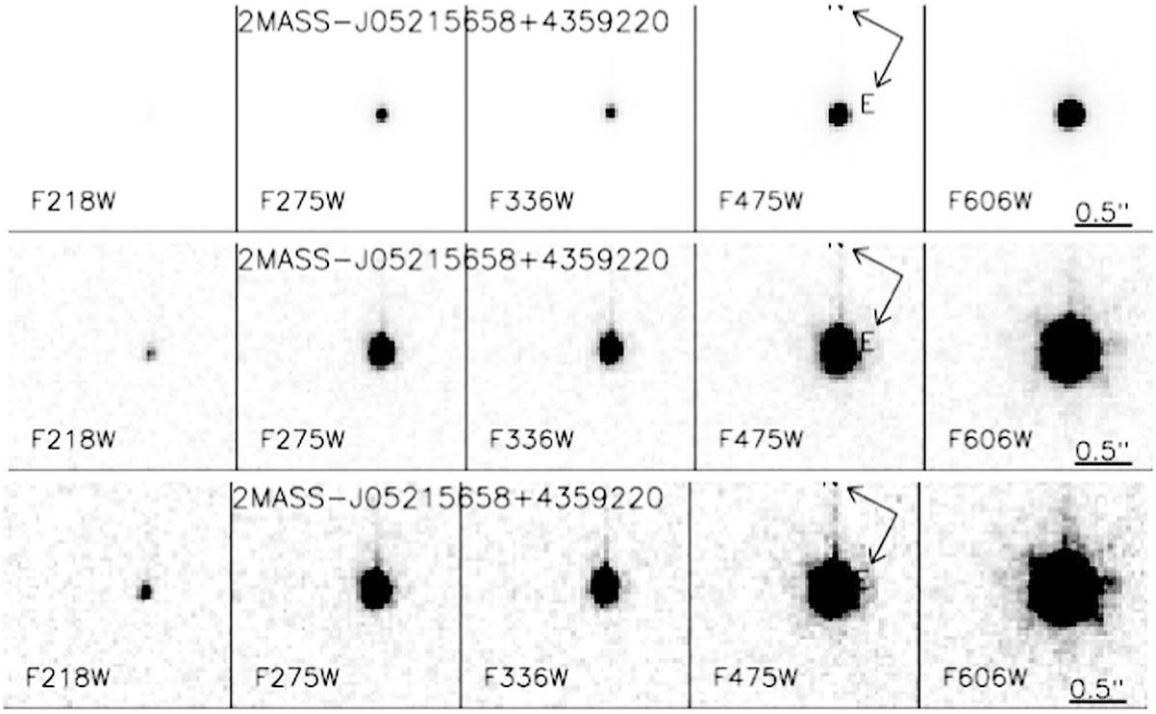

Figure 7. WFC3 images of the source in the five filters arranged from shorter to longer effective wavelength; repeated in different rows using increasing contrast. Images are 50 × 50 pixel cutouts (one pixel is 0.″04). For the dithered exposures, the pictures were produced from the drizzled images, therefore the resolution is slightly degraded with respect to the full resolution of individual exposures.

evidence for a semi-resolved pair. There is no evidence in the residual images; for some images the subtraction of the detected source model is nearly perfect; in some cases a residual feature is seen but it is symmetric around the source, suggesting a mismatch of the PSF model rather than an extra component. From this objective analysis, and from visual inspection, the source appears unresolved. A WFC3 pixel (0.″04) at the distance of our target projects to ∼100 au on the sky (0.000477648 pc). Assuming that some separation or elongation would be detectable at a resolution of ∼2.5 pixels,

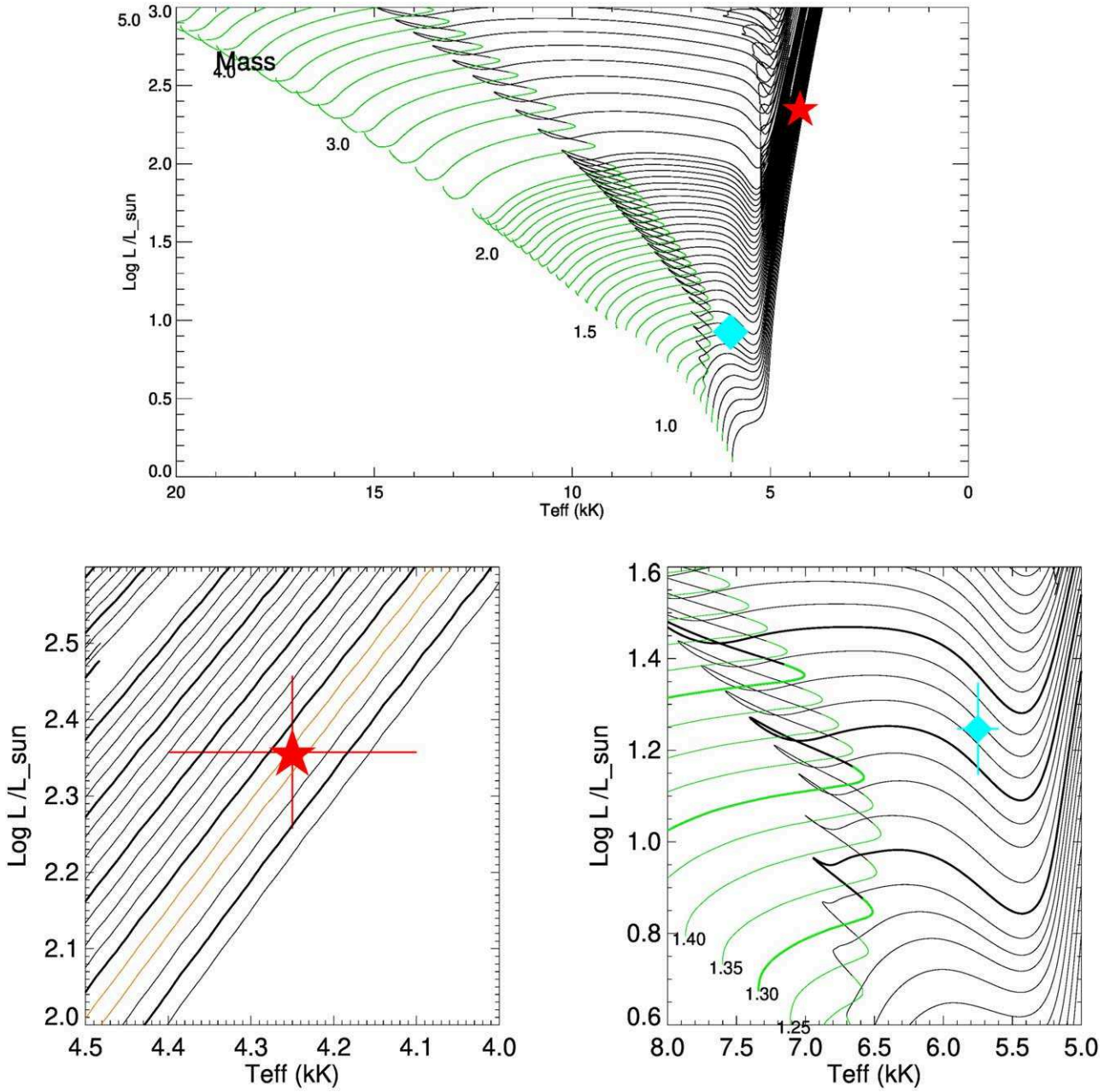

Figure 8. HR diagram of PARSEC evolutionary tracks for metallicity $Z = 0.006$; the main-sequence phase is shown in green. The red star marks the RG position, and the cyan diamond is the companion. The bottom panels zoom around the locus of each star: in the left panel (RG) tracks with masses of 0.9, 1.1, 1.3, 1.5, and $1.7 M_{\odot}$ (from the bottom right toward the top left) are marked with thick black lines, and tracks for masses of 1.0 and $1.05 M_{\odot}$ are shown in orange; in the right-bottom panel, thick-line tracks have masses of 1.3, 1.5, and $1.7 M_{\odot}$.

i.e., 0.″1, an unresolved source implies an upper limit to the orbital separation of $\boldsymbol{a} \times \sin(i) \leqslant 246$ au, or $\leqslant 1891$ RG radii (using the value of $R_{\rm RG} = 28 R_{\odot}$ derived in Section 3.2.1), much larger than is estimated for this pair (Section 4). In sum, the broadband photometry was planned in order to acquire a very deep SED measurement in a short time (one orbit only), in case the STIS exposures failed. The lack of close neighbors in the images further confirms the association of the target with the Gaia counterpart.

3.5. Current Stellar Masses and Evolutionary Implications

In Figures 8 and 9 the stellar parameters derived in Section 3.2.2 for both the RG and the subgiant companion are compared with PARSEC evolutionary tracks (A. Bressan et al. 2012 and subsequent updates) for $Z = 0.006$ and $Z = 0.002$. The tracks are sampled with fine mass steps in the mass range of the target; to distinguish them in the complex region of the loops we show them with different colors and thicknesses, as explained in the figure caption. The plotted uncertainty in $\log(L_{\rm bol}/L_{\odot})$ is ≈ 0.1 (0.06 from the $T_{\rm eff}$ uncertainty and 0.04 from the distance uncertainty, which directly translates into uncertainty in the radius value). However, as shown in Figures 2–4, for the lower-metallicity solution a smaller radius and slightly hotter temperature are found for the companion. Therefore, the two distinct solutions are shown in separate figures. The comparison with tracks for $Z = 0.006$ (one-third solar) indicates a red giant mass of around

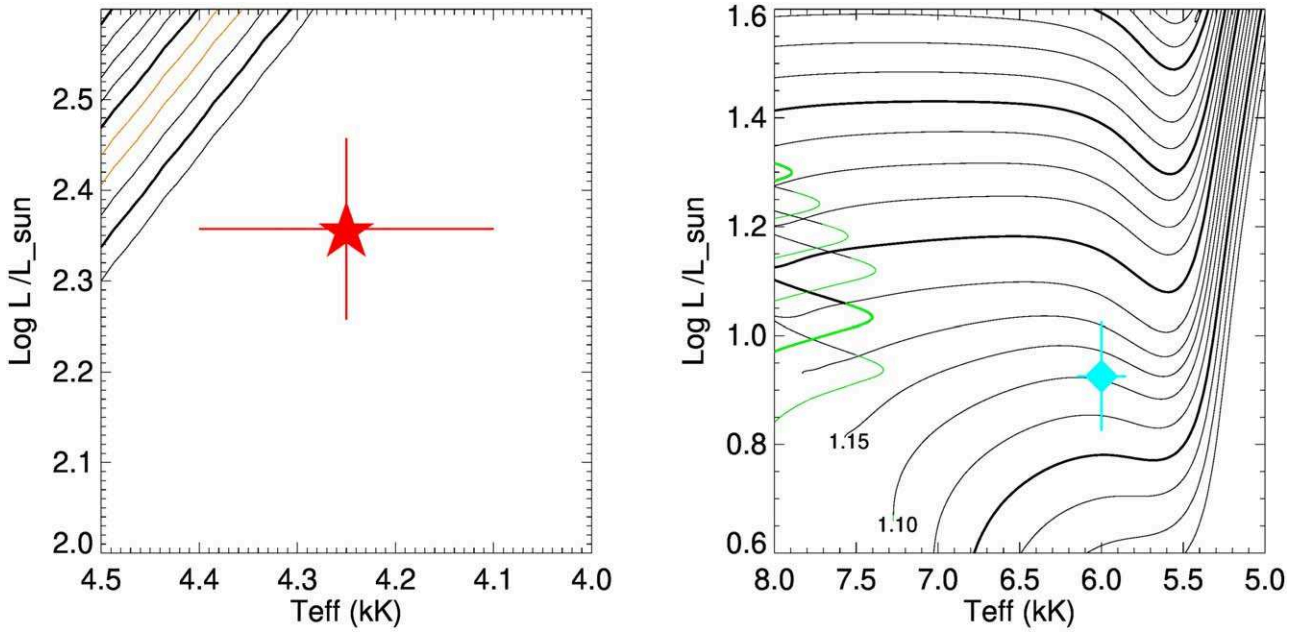

Figure 9. HR diagram of PARSEC evolutionary tracks for metallicity $Z = 0.002$; the main-sequence phase is shown in green. The red star marks the RG position and the cyan diamond the companion, using the parameters derived with models of metallicity $Z = 0.002$ (Figure 2). In the left panel, the loops of the evolutionary tracks do not reach the $T_{\rm eff}$ derived for the RG; in the right panel, thick-line tracks have masses of 1.0, 1.3, and $1.5 M_{\odot}$.

$1 M_{\odot}$ (between 1.35 and $0.85 M_{\odot}$), and a subgiant companion mass of $\approx 1.6 \pm 0.1 M_{\odot}$. The PARSEC tracks for metallicity of one-tenth of the solar value does not extend to $T_{\rm eff}$ values as low as the RG's estimated $T_{\rm eff}$, but the trend indicates that the inferred mass would then be lower than $1 M_{\odot}$, and the companion's mass of $\sim 1.1 \pm 0.1 M_{\odot}$.

4. Discussion and Summary

We investigated the nature of the binary system 2MASS J05215658+4359220. In particular, this work adds new data in the UV range to the existing abundant data and analyses, and conclusively reveals a red giant's companion, whose nature was still debated. No data existed in the FUV range for the source. To test the possible presence of a hot compact companion (Section 3.1), we obtained Astrosat/UVIT imaging in two filters at FUV wavelengths. To test other scenarios and in particular the presence of a main-sequence star hotter but less luminous than the RG, we obtained HST/STIS spectra and HST/WFC3 high-resolution imaging from the UV to the near-IR range.

A hot, low-optical-luminosity stellar companion is ruled out by 2σ upper limits obtained in FUV imaging with Astrosat/UVIT ($\geqslant$25.8 ABmag in FUV.F1 and $\geqslant$25.7 ABmag in FUV.F3) and HST/STIS (flux upper limit of 10^{-17} erg cm^{-2} s^{-1} Å^{-1} shortwards of 2300 Å).

The broad wavelength range HST/STIS spectrum from 1600 to 10230 Å is well matched by the sum of two stellar models: the RG primary with $T_{\rm eff} = 4250$ K, $\log g = 2.0$, $R_{\rm RG} = 27.9 R_{\odot}$, $\log(L_{\rm bol}/L_{\odot}) = 2.36 \pm 0.1$, and a companion with $T_{\rm eff} = 6000$ K, $\log g = 3.0$, $R_{\rm comp} = 2.7\, R_{\odot}$, and $\log(L_{\rm bol}/L_{\odot}) = 0.925 \pm 0.1$ for metallicity of one-tenth the solar value. Extinction was constrained to $E_{B-V} = 0.50 \pm 0.02$ mag. Such a combination was found to best match the major absorption features in the UV range (see the bottom panel in Figures 2 and 4) and the overall flux distribution. Using models with metallicity one-third solar, closer to the findings by T2019 and K. El-Badry et al. (2024, in preparation) from ground-based spectra, the whole flux distribution is matched with similar parameters for the RG ($R_{\rm RG} = 27.78 R_{\odot}$), but slightly different for the companion: $T_{\rm eff} = 5750$ K, $R_{\rm comp} = 4.2 R_{\odot}$, and $\log(L_{\rm bol}/L_{\odot}) = 1.25 \pm 0.1$. The continuum SED is still well matched, although some broad absorption bands are less well matched compared to the lower-metallicity model (see Figure 4 in particular). The derived stellar parameters for the RG are consistent with the line analysis on high-resolution, high-S/N Keck spectra where lines from both stellar components can be resolved (K. El-Badry 2024, private communication). The UV spectra and the analysis of the absolute-flux SED over the entire STIS spectral range allowed us to refine the companion's parameters and the foreground extinction, which in turn enables derivation of stellar radii from the extinction-corrected fluxes, adopting the Gaia DR3 distance of $D = 2463$ pc with a 5% error. The solution could be further refined if more precise metallicity values and $\log g$ will be constrained from high-resolution spectra, which should be feasible at least for the RG.

Mg II λ2800 Å emission from the RG indicates chromospheric activity comparable to that of active RGs. In 2MASS J05215658+4359220, measurement of the line emission must account for the companion's flux contribution that overwhelms the RG flux at these wavelengths (Figures 4 and 6), making the Mg II emission appear lower than it actually is.

The STIS spectra, and the UV range in particular, allowed us to conclusively detect and to constrain the nature and the stellar parameters of a hotter, lower-luminosity companion simultaneously with the RG primary. However, our HST observations sample only one phase. No orbital-related variability has been explored in UV as yet, while ample literature reports variability in V-mag and RV of the RG (K. El-Badry et al. 2024, in preparation and references therein). The STIS fluxes, convolved with the GALEX transmission curves, give NUV magnitudes consistent with the measurements in the GALEX archive, but only repeated STIS spectra at selected optical

phases can reveal variability (if any) of the hotter component of the system. K. El-Badry et al. (2024, in preparation) have also reanalyzed the available photometric data of the target (V and g bands) between 2015 and 2022; the light curves show a 20% total amplitude flux variation in the V band up until 2018, then the variability (analyzed by folding the data with the orbital period) seems to have subsided or become more complex in recent years (K. El-Badry 2024, private communication). Similarly, a complex variation over timescales of years of the optical light curve (folded with the orbital $P = 82.2$ days) was illustrated by T2019. According to our spectrum decomposition shown in Figures 2 and 3, the companion flux is 0.6% or 6.3% (using models with $Z = 0.002$ or $Z = 0.006$, respectively) of the RG's flux at the longest wavelengths ($\sim$10000 Å); it becomes $\sim$17% or 32% of the total flux shortwards of 4000 Å, and it is the predominant source of flux shortwards of $\approx$3000 Å. Around 5000 Å, the companion's flux is $\lesssim$10% of the total flux, which is essentially the RG's flux. Therefore, in principle, its contribution is comparable at most to the reported amplitude of the flux variations in the V band. However, the ellipsoidal shape of the light curves, shown by K. El-Badry et al. (2024, in preparation) and by T2019, suggests—as these authors have proposed and demonstrated—that the variability is due to azimuthal asymmetry (and spot activity?) of the RG's surface in a locked rotation-orbital motion. The possibility of a significant distortion or spot activity on the RG surface raises the concern that the spectral decomposition assuming a single-temperature spectrum for the RG may be an approximation. A more detailed investigation, accounting for possible azimuthal variations of the RG surface, can be performed on phase-dependent spectra analyzed with updated orbital parameters, and it is not possible with the current single-epoch spectra. The companion, according to our STIS spectral decomposition, has a much smaller radius than the RG, and the addition or eclipsing of its flux with orbital phase (assuming an edge-on view) would likely cause a flat-bottom dip in the light curve. In sum, a smaller, hotter subgiant companion might be at the other orbital focus from the RG, but we cannot entirely rule out yet the possibility that the RG and the subgiant are a very close pair that underwent recent mass exchange and might be on their way to coalescing, both locked together and orbiting a third body. Repeating the STIS spectra at sample orbital phases would show whether the UV-emitting source is moving in phase, or rather antiphase, with the RG orbit, or moving with it around a third mass. While investigating variations of the UV flux with Hubble is easily doable, RV measurements of the companion would require a much larger telescope, and high-resolution spectra in the blue range.

The masses from our spectral decomposition, $M_{\rm RG} \sim 1 M_{\odot}$ and $M_{\rm comp} \sim 1.6 M_{\odot}$, combined with the orbital period of $P_{\rm orb} = 82.2$ days, imply an orbital separation $\boldsymbol{a} = 0.51$ au or $\sim 110 R_{\odot}$, i.e., about $4 \times R_{\rm RG}$. For the solution yielding $M_{\rm comp} \sim 1.1 M_{\odot}$, $\boldsymbol{a} = 0.48$ au, i.e., $\sim 103\, R_{\odot}$, $3.7 \times R_{\rm RG}$. The radius of the RG's orbit would be $\boldsymbol{a}_{\rm RG} = 0.32$ au, $2.4 \times R_{\rm RG}$, from our derived mass ratio, fairly consistent with the value derived from P and RV amplitude, $\boldsymbol{a}_{\rm RG} = 0.34$ au, and implying, as found in previous works, that currently the RG is not filling its Roche lobe. Such a small separation also favors a distortion of the RG surface, and may explain the temperature and luminosity difference between the hemisphere facing the companion and the opposite one, as seen by T12019 and K. El-Badry et al. (2024, in preparation). The subgiant companion's RV amplitude should then be $\sim$27.8 km s^{-1} (for mass ratio 1/1.6), or 40.5 km s^{-1} for mass ratio 1/1.1. If both stars were instead orbiting around a third mass, i.e., if we suppose that the RG and the subgiant are a coalescing pair orbiting with RV amplitude of 44.5 km s^{-1} around the postulated BH, the orbit radius of the RG $\boldsymbol{a}_{\rm RG} = 0.34$ au (from the published P and RV values) would imply a mass of $2.8 M_{\odot}$ at the other focus, and a total separation of 0.65 au. Such a scenario would explain the estimated mass function that suggests a mass lower limit for the undetected companion of $2 M_{\odot}$ (T2019; K. El-Badry 2024, private communication), larger than what our spectroscopic analysis suggests for the subgiant.

The main result from this work is the definitive detection of a stellar companion, a subgiant hotter and slightly more massive than the RG primary, implying recent mass transfer from the RG, and removing the need (but not the possibility) to postulate a BH companion for one of the rare standing candidate noninteractive BH binary systems. The simultaneous space-based (absolute flux calibrated) spectroscopy from $\sim$1600 to 10230 Å uniquely enabled the derivation of stellar parameters for the two stars, and in particular for the hotter companion, which is elusive at optical wavelengths where fluxes are dominated by the RG. However, confirmation that the pair is only comprised of these two components, and that the NUV-emitting source is not a close (possibly merging) companion to the RG, with a third mass on a wider orbit, could only come from phase monitoring of the UV fluxes, and modeling of high-resolution line spectra in the blue range. Our initially postulated additional alternative that the NUV flux may arise from an accretion disk, unlikely given the lack of X-ray emission (VdHT20), seems further dismissed by the lack of FUV flux and the presence of absorption bands in the STIS NUV spectra (Figure 4), by comparison with common accretion disk models and studies (e.g., R. Puebla et al. 2007; I. Hubeny & K. S. Long 2021 and references therein). These results also make this source a valuable benchmark for testing binary stellar evolution theories, given the unusual abundance of data and precise measurements, augmenting the scant existing well-studied sample of stripped RG binaries (e.g., K. El-Badry et al. 2022).

The current results indicate that the RG is probably not filling its Roche lobe, although optical light variability locked with orbital phase (T2019 and references therein) is likely a relic of recent interaction, as is also implied from the mass ratio and from the chromospheric emission shown in this work. Precise abundance constraints from high-resolution line analysis would critically reduce the uncertainty in the current mass estimates.

5. Publicly Available Data

Please reference this publication if using the data below.

1. The extracted STIS spectra, combined for the three gratings, can be downloaded from Zenodo doi:10.5281/zenodo.14051646 (filename: STIS_2mj05215.mrg) or by direct link from our website: http://dolomiti.pha.jhu.edu/uvsky/RGbinary_2MASSJ05215658+4359220/STISspectra/STIS_2mj05215.mrg. The ascii file includes the three-ranges spectra extracted and combined: G230L+G430L+G750L.

Columns are as follows: WAVELENGTH (Å), COUNT-RATE (counts cm^{-2} s^{-1} $pixel^{-1}$), FLUX (erg cm^{-2} s^{-1} $Å^{-1}$), STAT-ERROR (erg cm^{-2} s^{-1} $Å^{-1}$), SYS-ERROR (erg cm^{-2} s^{-1} $Å^{-1}$), NPTS (the number of coadded spectra for that pixel), TIME (total exposure time at that pixel in seconds), QUAL (1 = good data, 0 = possibly poor data quality). The original HST data products, which are not the re-extracted spectra available here, are available at MAST, doi:10.17909/tvvw-4e47.

2. The UVIT images, reconstructed from the photon-counting archival data, calibrated accounting for dead-time corrections, can be downloaded from Zenodo, doi:10.5281/zenodo.14051646 (filename: UVITimages.tar) or by direct link from our website:http://dolomiti.pha.jhu.edu/uvsky/RGbinary_2MASSJ05215658+4359220/UVITimages/UVITimages.tar. The tar file contains the following .fits files of the reconstructed images, where the "NORM_EXPARRAY" files are the normalized relative response maps across the field, expressed as 0 to 1. So, the effective exposure time at a pixel position is RDCDTIME multiplied by this image. The "NORMEXP_IMAGE" is the science image, which must be divided by the product of RDCDTIME and the NORM_EXPARRAY image on a pixel-by-pixel basis to obtain counts s^{-1} $pixel^{-1}$.

2MASSJ05215658+4359220_FUV_CaF2___MASTER_NORM_EXPARRAY_A10_093T01_9000004128.fits
2MASSJ05215658+4359220_FUV_CaF2___MASTER_NORM_EXPARRAY_A10_093T01_9000004266.fits
2MASSJ05215658+4359220_FUV_CaF2___MASTER_NORM_EXPARRAY_Merged.fits
2MASSJ05215658+4359220_FUV_CaF2___MASTER_NORMEXP_IMAGE_A10_093T01_9000004128.fits
2MASSJ05215658+4359220_FUV_CaF2___MASTER_NORMEXP_IMAGE_A10_093T01_9000004266.fits
2MASSJ05215658+4359220_FUV_CaF2___MASTER_NORMEXP_IMAGE_Merged.fits
2MASSJ05215658+4359220_FUV_Sapphire___MASTER_NORM_EXPARRAY_A10_093T01_9000004128.fits
2MASSJ05215658+4359220_FUV_Sapphire___MASTER_NORM_EXPARRAY_A10_093T01_9000004266.fits
2MASSJ05215658+4359220_FUV_Sapphire___MASTER_NORM_EXPARRAY_Merged.fits
2MASSJ05215658+4359220_FUV_Sapphire___MASTER_NORMEXP_IMAGE_A10_093T01_9000004128.fits
2MASSJ05215658+4359220_FUV_Sapphire___MASTER_NORMEXP_IMAGE_A10_093T01_9000004266.fits
2MASSJ05215658+4359220_FUV_Sapphire___MASTER_NORMEXP_IMAGE_Merged.fits

Acknowledgments

L.B. and D.T. acknowledge support from grant No. HST-GO-16654. L.B. is very grateful to the UVIT support team and to the HST program scientists for help in optimizing and executing the approved observations and to Joe Postma for reconstructing the UVIT images with his s/w package. L.B. is extremely grateful to Kareem El-Badry, who shared results from his high-resolution, high-S/N Keck spectra prior to publication, and provided most helpful and generous discussions on the nature of the system. E.B. is supported by NSF grant No. AST-2307146 and by the Simons Foundation.

Facilities: Astrosat (UVIT), HST (STIS), HST (WFC3), GALEX, MAST, Gaia.

ORCID iDs

Luciana Bianchi https://orcid.org/0000-0001-7746-5461
Ralph Bohlin https://orcid.org/0000-0001-9806-0551
Emanuele Berti https://orcid.org/0000-0003-0751-5130

References

Abadie, K., Abbott, B. P., Abbott, R., et al. 2010, CQGra, 27, 173001
Abbott, B. P., Abbott, R., Abbott, T. D., et al. 2016, ApJL, 818, L22
Abbott, B. P., Abbott, R., Abbott, T. D., et al. 2017a, ApJL, 848, L12
Abbott, B. P., Abbott, R., Abbott, T. D., et al. 2017b, ApJL, 848, L13
Abbott, B. P., Abbott, R., Abbott, T. D., et al. 2017c, PhRvL, 119, 161101
Antoniadis, J., Tauris, T., Ozel, F., et al. 2016, arXiv:1605.01665
Banerjee, S. 2018, MNRAS, 481, 5123
Bianchi, L. 2024, ApJS, 274, 45
Bianchi, L., Kang, Y., Hodge, P., Dalcanton, J., & Williams, B. 2014, AdSpR, 53, 928
Bianchi, L., & Shiao, B. 2020, ApJS, 250, 36
Bressan, A., Marigo, P., Girardi, L., et al. 2012, MNRAS, 427, 127
Castelli, F., & Kurucz, R. L. 2003, in IAU Symp. 210, Modelling of Stellar Atmospheres, Poster Contributions, ed. N. Piskunov, W. W. Weiss, & D. F. Gray (San Francisco, CA: ASP)
D'Orazio, D. J., & Samsing, J. 2018, MNRAS, 481, 4775
El-Badry, K., Seeburger, R., Jayasinghe, T., et al. 2022, MNRAS, 512, 5620
Hubeny, I., & Long, K. S. 2021, MNRAS, 503, 5534
Langer, N., Schürmann, C., Stoll, K., et al. 2020, A&A, 638, 39
Moe, M., & di Stefano, R. 2017, ApJS, 230, 15
Ozel, F., Psaltis, D., Narayan, R., & McClintock, J. E. 2010, ApJ, 725, 1918
Ozel, F., Psaltis, D., Narayan, R., & Santos Villarreal, A. 2012, ApJ, 757, 550
Patrick, L. R., Lennon, D. J., Britavskiy, N., et al. 2019, A&A, 624, 129
Postma, J. E., & Leahy, D. 2021, JApA, 42, 30
Postnov, K. A., & Yungelson, L. R. 2006, LRR, 9, 6
Puebla, R., Diaz, M. P., & Hubeny, I. 2007, AJ, 134, 1923
Sana, H., Bouquin, J. B., Lacour, S., et al. 2014, ApJS, 215, 15
Sana, H., Ramirez-Tannus, M. C., de Koter, A., et al. 2017, A&A, 599, L9
Strassmeier, K. G. 2009, A&ARv, 17, 251
Tandon, S. N., Postma, J., Joseph, P., et al. 2020, AJ, 159, 158
Thompson, T., Kochanek, C., Stanek, K., et al. 2020, Sci, 368, eaba4356
Thompson, T. A., Kochanek, C. S., Stanek, K. Z., et al. 2019, Sci, 366, 637
van den Heuvel, E. P., & Tauris, T. M. 2020, Sci, 368, eaba3282